Theory of strain-induced confinement in transition metal dichalcogenide monolayers

Matthew Brooks* and Guido Burkard
Department of Physics, University of Konstanz, D-78464 Konstanz, Germany

(Received 26 March 2018; published 31 May 2018)

Recent experimental studies of out-of-plane straining geometries of transition metal dichalchogenide (TMD) monolayers have demonstrated sufficient band-gap renormalization for device application, such as single-photon emitters. Here, a simple continuum-mechanical plate-theory approach is used to estimate the topography of TMD monolayers layered atop nanopillar arrays. From such geometries, the induced conduction-band potential and band-gap renormalization are given, demonstrating a curvature of the potential that is independent of the height of the deforming nanopillar. Additionally, with a semiclassical WKB approximation, the expected escape rate of electrons in the strain potential may be calculated as a function of the height of the deforming nanopillar. This approach is in accordance with experiment, supporting recent findings suggesting that increasing nanopillar height decreases the linewidth of the single-photon emitters observed at the tip of the pillar and predicting the shift in photon energy with nanopillar height for systems with consistent topography.

DOI: 10.1103/PhysRevB.97.195454

I. INTRODUCTION

Transition metal dichalchogenide (TMD) monolayers are atomically thin semiconducting crystals boasting optically active direct band gaps and strong spin-orbit coupling which in turn introduces optically addressable spin-valley coupling [1–4]. Chemically, semiconducting TMD monolayers are described as MX_2, consisting of one transition metal atom $M =$ Mo or W for every two chalcogen atoms $X =$ S or Se arranged in a staggered hexagonal two-dimensional (2D) lattice, similar to graphene but with a broken inversion symmetry. This allows for the electrons to possess the time-reversal symmetric valley-isospin degree of freedom (K/K'), whereas the broken inversion symmetry opens a direct optical range band gap about these valleys. Additionally, the transition metal atoms introduce a strong spin-orbit coupling, correlating the spin and valley degrees of freedom, forming twofold-degenerate Kramers pairs $|K\uparrow\rangle/|K'\downarrow\rangle$ and $|K'\uparrow\rangle/|K\downarrow\rangle$. Since monolayer isolation, a number of possible devices exploiting the novel spin-valley and 2D material physics have been theorized and demonstrated. These include low-dimensional van der Waals heterostructure field-effect transistors [5–7], photovoltaic systems, photodetectors [8–10], as well as spintronic [11–13] and valleytronic [14–16] devices.

Several standard material manipulation and combination techniques have already become part of the standard toolbox of monolayer engineering, including metal electrode gating and layered heterostructure composites [5–8,10–16]. Recently, a number of studies into out-of-plane straining as a novel manipulation technique have been experimentally investigated for deterministically implementing quantum light sources [17–19]. Similar to other low-dimensional crystals, such as graphene and hexagonal boron nitride, TMDs exhibit great flexibility and mechanical strength. It is known that TMD monolayers can withstand tensile strain up to the order of 10% [20] before rupture, thus the ongoing interest in TMDs for flexible substrate technologies [21,22]. As such, there have been notable density functional theory (DFT) studies into the electronic response of TMD monolayers to tensile strain [23,24]. Interestingly, it is believed that all TMD species form a type-II quantum well (electron confining but hole repulsive) of the conduction and valence bands under strain with the exception of WSe_2 which forms type-I quantum dots (QDs) (electron and hole confining). One noticeable change in the behavior of specifically sulphide semiconducting TMDs (MS_2) under strain is a direct to indirect band-gap transition that has been observed at 2.5% tensile strain in WS_2 [25] and calculated to be at about 2% for MoS_2 [23].

Single-photon emitters (SPEs) had previously been observed in a TMD monolayer at strained defect points along the edge of a monolayer flake [26]. With out-of-plane straining, this effect has now been shown to be deterministically implementable by creating strain fields with an appropriate renormalization of the band gap to funnel excitons to a given location in WSe_2 by placing the TMD on a substrate that selectively deforms the monolayer. Similarly, it has previously been suggested that an atomic force microscope (AFM) tip may be used to strain MoS_2 monolayers for electron collection in photovoltaic devices [9]. It is clear that the flexibility, strain band response, and durability of TMD monolayers opens up the novel device implementation tool of strain manipulation by exploiting the third dimension of a 2D material. Out-of-plane strain field engineering has the potential to become part of the standard toolbox of TMD device implementation to be used as an additional tool to help manipulate the conduction and valence bands. The potential for strain engineering for quantum emitters is now well demonstrated, but a similar method could be combined with other known manipulation techniques to allow for hybrid strain-gated electronic devices.

It is the goal of this paper to develop a satisfying approximate analytical model of the TMD topography due to

*matthew.brooks@uni-konstanz.de

a deforming element, such as a nanopillar grown from a substrate. Thereafter the strain-induced potentials from such geometries will be calculated, and predictions of the band-gap renormalization, single-particle energy spectra, and probability of tunneling out of the strain-defined potential region will be made.

This paper is structured as follows. An analytical description of a TMD monolayer deformed about a nanopillar grown out of a silica substrate is theoretically derived in Sec. II followed by an analysis of the strain-induced potential from the derived deformation in Sec. III. In Sec. IV the energy levels of electrons confined by the strain-induced potential are given, and in Sec. V the semiclassical WKB approximation is used to estimate electron leakage from the given potentials. Finally, a discussion of the possible devices single-particle strain-induced potential wells allow is provided in Sec. VI, and a summary of the presented paper is given in Sec. VII.

II. DEFORMATION TOPOGRAPHY

In this paper we calculate the out-of-plane deformation topography of the TMD monolayers layered atop nanopillars using continuum-mechanical plate theory. The full set of elastostatic equilibrium equations [27] assuming rotational symmetry are

$$D\Delta^2\zeta - \frac{h}{r}\left(\frac{d\chi}{dr}\frac{d^2\zeta}{dr^2} + \frac{d^2\chi}{dr^2}\frac{d\zeta}{dr}\right) = P, \tag{1a}$$

$$\Delta^2\chi + \frac{E}{r}\left(\frac{d\zeta}{dr}\frac{d^2\zeta}{dr^2}\right) = 0, \tag{1b}$$

where ζ is the deformation coordinate (height field) of the TMD, χ is the stress function, h is the thickness of the TMD, E is the Young's modulus, P is the externally applied force per unit area, and D is the flexural rigidity of the TMD defined as

$$D = \frac{Eh^3}{12(1-\sigma^2)}, \tag{2}$$

where σ is Poisson's ratio. The stress function χ is defined as

$$\Delta\chi = \frac{E}{(1-\sigma)}\nabla\cdot\mathbf{u} = \frac{E}{(1-\sigma)}\left(\frac{1}{r}\frac{d(ru_r)}{dr}\right), \tag{3}$$

where $\mathbf{u} = (u_r, u_\theta)$ is the displacement vector. Note that $\Delta = \nabla^2$ where Δ is the Laplacian operator and ∇ is the gradient whereas Δ^2 is the biharmonic operator. The first of these equations (1a) is derived from energetic considerations whereas the second (1b) describes the stress-strain relationship. In this paper, we study similar topographies to those used in experiments where the TMD monolayer is passively strained (lacking clamping of the edges and allowing for elastic equilibrium). In such a regime, the contribution from the stress function to the overall strain in the TMD will be five orders of magnitude lower than that of the contribution from the height-field topography. As such, a pure bending regime is assumed where the elastostatic equations may be simplified to

$$D\Delta^2\zeta - P = 0, \tag{4}$$

where (1b) may no longer be satisfied.

There are a number of choices for force per unit area to be considered; $P = 0$ with boundary conditions, van der Waals attraction between the TMD and the substrate [28],

$$P_{\mathrm{VDW}} = \frac{\mathcal{H}_{\text{TMD-Sub}}}{(h/2+\zeta)^3}, \tag{5}$$

where $\mathcal{H}_{\text{TMD-Sub}}$ is the Hamaker constant between the choice TMD and substrate and a constant force per unit area $P = P_c$ approximation. The van der Waals force topography may be calculated numerically whereas the height fields of the $P = 0$ and $P = P_c$ models may be exactly solved to give

$$\zeta_{P=0}(r) = \frac{H\left(R^2 + r^2\left[\ln\left(\frac{r^2}{R^2}\right) - 1\right]\right)}{R^2}, \tag{6}$$

and

$$\zeta_{P=P_c}(r) = \begin{cases} \beta\left(\sqrt{\frac{H}{\beta}} - r^2\right)^2, & r \leqslant R, \\ 0, & r > R, \end{cases} \tag{7}$$

respectively, where H is the height of the deforming nanopillar, i.e., the height at which the TMD is held at at the origin, R is the tenting radius, i.e., the radius at which the TMD meets the substrate, and β is defined as

$$\beta = \frac{P_c}{64D} = \frac{3P_c(1-\sigma^2)}{16h^3E}. \tag{8}$$

Both of these models for the height field assume "clamped" boundary conditions $\partial_r\zeta(r)|_{r=0,R} = 0$. The values of R and H need to be assumed for the $P = 0$ model as all mechanical properties of the TMD are lost, whereas for the $P = P_c$ model the relationship between R and H is given as $R = \sqrt[4]{H/\beta}$.

Figure 1 demonstrates the difference between the topographies given by the three proposed P functions. As is evident, the $P = P_c$ model aligns well with the $P = P_{\mathrm{VDW}}$ model close to the origin (where electron confinement takes place) whereas close to the tenting radius the $P = P_c$ model aligns with the $P = 0$ model. As such, the $P = P_c$ will be used to give a reasonable analytical approximation to experimental works which we aim to model.

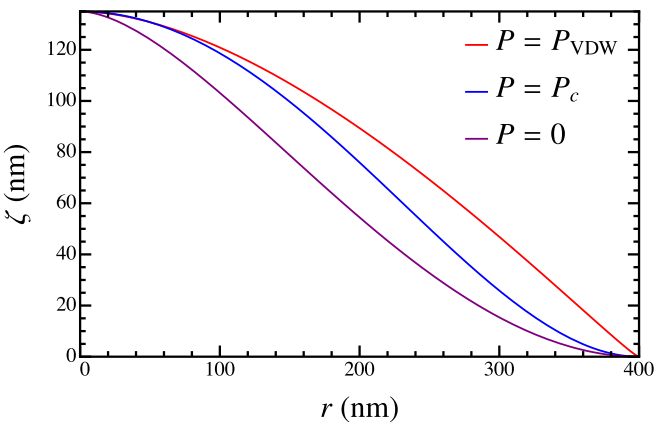

FIG. 1. Two-dimensional radial deformation topography of WSe_2 derived from the $P = 0$ (purple line), $P = P_c$ (blue line), and $P = P_{\mathrm{VDW}}$ (red line) assuming a nanopillar height of 135 nm with a tenting radius of 400 nm as chosen from experimental examples [17].

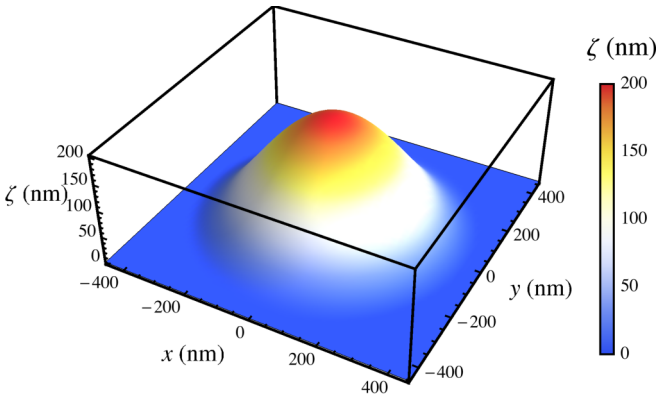

FIG. 2. Height-field $\zeta(x,y)$ as a function of the x and y coordinates on the TMD plane of a WSe_2 monolayer layered atop a 200 nm tall nanopillar.

This paper will focus on the TMD monolayer species of MoS_2 and WSe_2. WSe_2 is considered since it has been the focus of past TMD strain experiments [17–19] that measured quantum emitters in strained regions of the monolayer. WSe_2's optical response on- and off-resonance may be greatly enhanced [29] and, as has been shown in DFT studies [23], exhibits exciton funneling under strain. MoS_2 is also considered as this material has been studied for its possible spintronic and valleytronic applications, such as quantum dots [30] for quantum information [4,31], due to its relatively small spin-orbit splittings. Values for the Young's modulus [32,33], Poisson's ratio [34,35], and layer thickness [36,37] are all taken from mechanical experiments, whereas a reasonable value for the applied force is approximated from the tenting radii of a nanopillar strained TMD experimental study [17].

A deformation topography of WSe_2 and MoS_2 may be drawn (Fig. 2) and compared (Fig. 3), deformed by nanopillars within the height range of 50–200 nm. This range has been chosen to coincide with the experimental possibilities for nanopillar growth and should not strain the monolayers to the point of perforation. These topographies will lay the foundation for the band-gap renormalization and conduction-band potential calculations performed below.

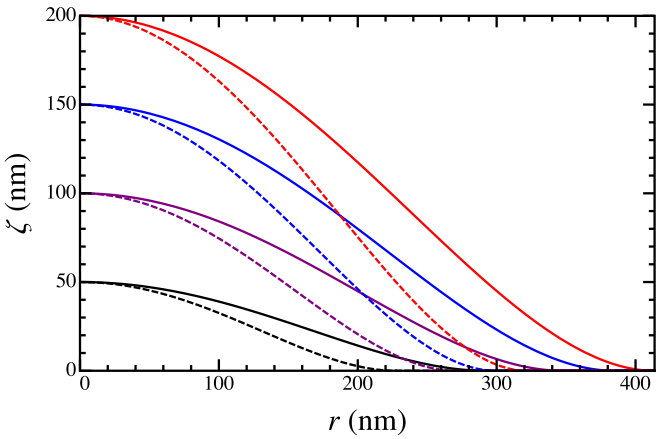

FIG. 3. Two-dimensional radial deformation topography of WSe_2 (solid lines) and MoS_2 (dashed lines) monolayers layered atop nanopillars of heights 50 nm (black lines), 100 nm (purple lines), 150 nm (blue lines), and 200 nm (red lines).

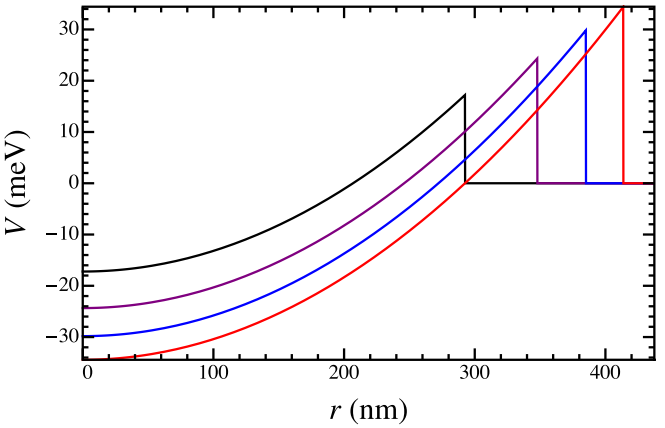

FIG. 4. Radial dependence of the strain-induced potential in the conduction band of WSe_2 monolayers deformed by nanopillars of heights 50 nm (black line), 100 nm (purple line), 150 nm (blue line), and 200 nm (red line). The curvature of the potential is unaffected by the pillar height whereas the depth depends on the height.

III. STRAIN-INDUCED POTENTIAL

With the deformed TMD monolayer topography derived in (7), the strain-induced potential is given as [38]

$$V = \begin{pmatrix} \delta_v \mathcal{D} & 0 \\ 0 & \delta_c \mathcal{D} \end{pmatrix}, \tag{9}$$

where δ_c and δ_v are the strain response parameters for the conduction and valence bands, respectively, and $\mathcal{D}$ is the trace of the strain tensor $\mathcal{D} = \mathrm{Tr}[\varepsilon_{ij}]$. In plate theory, the strain tensor is defined as [27]

$$\varepsilon_{ij} = \begin{pmatrix} -h\frac{\partial^2\zeta}{\partial x^2} & -h\frac{\partial^2\zeta}{\partial x\,\partial y} & 0 \\ -h\frac{\partial^2\zeta}{\partial x\,\partial y} & -h\frac{\partial^2\zeta}{\partial y^2} & 0 \\ 0 & 0 & \frac{\sigma h}{1-\sigma}\Delta\zeta \end{pmatrix}. \tag{10}$$

Using the above, $\mathcal{D} = \mathrm{Tr}[\varepsilon_{ij}]$ may be simplified to

$$\mathcal{D} = \frac{(2\sigma - 1)h}{1-\sigma}\Delta\zeta. \tag{11}$$

Therefore, the strain-induced potential in the conduction and valence bands from the derived topography has the following (truncated) harmonic form:

$$V_{c/v}(r) = \begin{cases} -\frac{8h\delta_{c/v}(2\sigma-1)(2r^2\beta-\sqrt{H\beta})}{\sigma-1}, & r \leqslant R, \\ 0, & r > R. \end{cases} \tag{12}$$

Notably, as can be seen in Fig. 4, the height of the deforming nanopillar does not affect the curvature of the induced potentials in the conduction and valence bands, yet does affect the overall band-gap shift (Fig. 5) and potential-well depth (Fig. 4), i.e., the difference in potential between $r = 0$ and $r > R$. Although our assumptions are modest, this result aligns with experiment [17] where the linewidth of single-photon emitters observed at the tip of deforming nanopillars was shown to scale with nanopillar height. In the experiment no discernible relationship between the nanopillar height and the emitted photon energies was observed, most likely due to the uncontrolled topographical variance between the observed

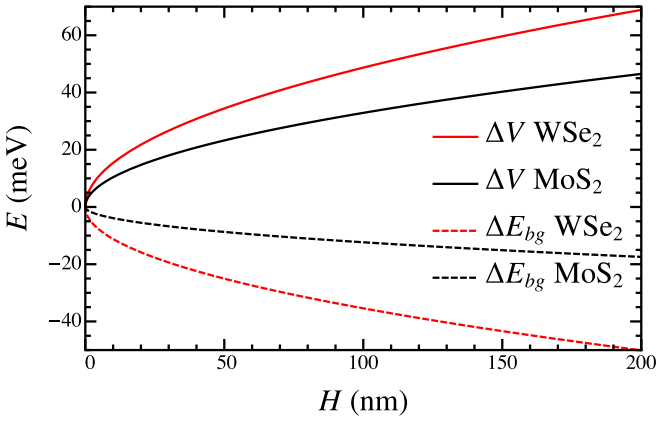

FIG. 5. Strain-induced potential-well height $\Delta V = V(r > R) - V(r = 0)$ in the conduction band (solid lines) and band-gap shift $\Delta E_{bg} = E_{bg} - [V_{cb}(r = 0) - V_{vb}(r = 0)]$ (dashed lines), induced by deforming nanopillars of height H for WSe_2 monolayers (red lines) and MoS_2 monolayers (black lines).

strain-induced quantum emitters. However, although the shifts in photon energy compared to unstrained monolayers seen experimentally are approximately equal to those predicted by the band-gap renormalization calculated, if the experimental systems offered greater consistency in topography with varying nanopillar height, we predict that there should be a shift in the photon energy by the predicted band-gap shift shown in in Fig. 5.

The quadratic form of this potential also allows for further extrapolations of the properties of the strained potential wells to be performed, such as an estimation of single-particle energy spectra and expected leakage. Other tight-binding approach studies of strain in TMDs [38,39] have shown the rise of fictitious gauge fields acting like pseudomagnetic fields on the plane of the monolayer due to curvature. In the systems considered here, this effect may be treated as a perturbation, as for these curvatures, the effective magnetic-field energy is on the order of $\sim\mu$eV, which is a few orders of magnitude below the confining potentials considered here.

IV. FOCK-DARWIN ENERGY LEVELS

From DFT studies [23], the behavior of the conduction and valence bands under strain for the four most common TMD species (MX_2 with M = Mo, W and X = S, Se) is well characterized. Notably, WSe_2 is the only compound which exhibits hole attraction, i.e., an increase in the valence-band energy about the $K(K')$ point, under strain. Conversely, the other three TMD species are believed to demonstrate hole repulsion, i.e., an increase in the valence-band energy at the $K(K')$ point, under strain. This is partly why WSe_2 has been the material of choice of optical strain experiments searching for quantum emitters in determined strained regions as the strain potential shape of both bands should allow for exciton funneling to a strain maximum. It can also be argued that strain-induced single-particle devices, such as quantum dots may be implemented in the other TMD types, such as MoS_2 [9] due to the hole repulsion.

Here we calculate the single-particle energy spectra of the strain-induced quantum dots, given deformed topography and induced strain potential described in Secs. II and III, in the presence of an external magnetic field. We begin by assuming the potential depth of the well described in (12) to be deep enough that a harmonic potential may be assumed. Then the Fock-Darwin energy levels of the quadratic portion of the potential may be obtained from the single-particle energy given by seven-band $k \cdot p$ theory analysis of an electron in a perpendicular magnetic-field B confined in a TMD monolayer [4], combined with the band-gap shift of (12). Thus the single band electron energy $E_{n,l}^{\tau,s}$ in a strain-induced potential with an external magnetic field is given as

$$E_{n,l}^{\tau,s} = E_{\mathrm{FD}} + E_{\mathrm{SO}} + E_{\mathrm{TRSV}} + E_{\mathrm{ZS}}, \tag{13}$$

where $\tau = \pm 1$ labels the valley-isospin $K(K')$, respectively, $s = \pm 1$ labels the electron spin $\uparrow$ ($\downarrow$) along the z direction, respectively. In 13, E_{FD} gives the Fock-Darwin energy levels of a 2D harmonic potential quantum dot defined by the strain potential,

$$E_{\mathrm{FD}} = (n+1)\sqrt{\frac{(\hbar\omega_c^{\tau,s})^2}{4} - \frac{32\hbar^2 h\beta\delta_c(2\sigma-1)}{m_{\mathrm{eff}}^{\tau,s}(\sigma-1)}} - \frac{\hbar\omega_c^{\tau,s} l}{2} + \frac{8h\delta_c(2\sigma-1)\sqrt{H\beta}}{\sigma-1}, \tag{14}$$

where $\omega_c^{\tau,s}$ is the cyclotron frequency given by the valley- and spin-dependent effect mass $m_{\mathrm{eff}}^{\tau,s}$. E_{SO} gives the energy splitting due to spin-orbit coupling of the Kramers pairs,

$$E_{\mathrm{SO}} = \tau s \Delta_{cb}, \tag{15}$$

where Δ_{cb} is the splitting in the conduction band about the $K(K')$ points. E_{TRSV} gives the of the valley degeneracies due to the violations of time-reversal symmetry,

$$E_{\mathrm{TRSV}} = \frac{(1+\tau)\mathrm{sgn}(B)}{2}\hbar\omega_c^{\tau,s}, \tag{16}$$

and finally E_{ZS} gives the valley and spin Zeeman splittings,

$$E_{\mathrm{ZS}} = \frac{\mu_B B}{2}(\tau g_v + s g_s), \tag{17}$$

where g_v is the valley-Zeeman splitting g factor and g_s is the spin-Zeeman splitting g factor. The quantum numbers are the principal quantum number $n = 0,1,2,\ldots$, which is defined as $n = 2n_r + |l|$ with the radial quantum number n_r of the wave function and the azimuthal quantum number $l = -n, -n+2, \ldots, n-2, n$.

The energy spectra with out-of-plane magnetic field of the first few states in MoS_2 is shown in Fig. 6. The larger spin-orbit splitting and lower magnetic response in WSe_2 give rise to a relatively unchanged magnetic spectrum when compared to other confinement methods in TMD monolayers. However, the MoS_2 levels demonstrate greater magnetic sensitivity than those derived for quantum dots assuming a hard wall potential of electrostatic gating [4] with clear Landau levels present at magnetic-field strengths of $\sim$5 T.

Notably, the energy spectra depicted here are calculated with constants mimicking previous experimental setups [17]. As such, the dots assumed are particularly large (~ 1 μm in diameter), which limits some of their potential for single-particle

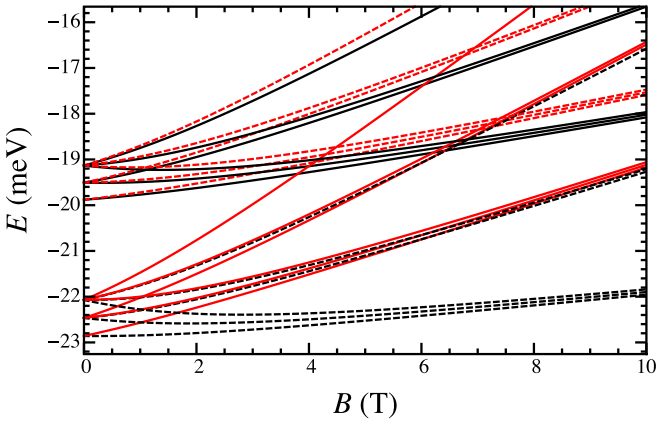

FIG. 6. Fock-Darwin energy spectra with external perpendicular magnetic-field B of an electron confined within the strain-induced potential well of an MoS_2 monolayer deformed by a nanopillar of height 200 nm up to $n = 2$, $l = \pm 2,0$. Here, the $K(K')$ states are given by the black (red) lines and the $\uparrow$ ($\downarrow$) states are given by the solid (dashed) lines.

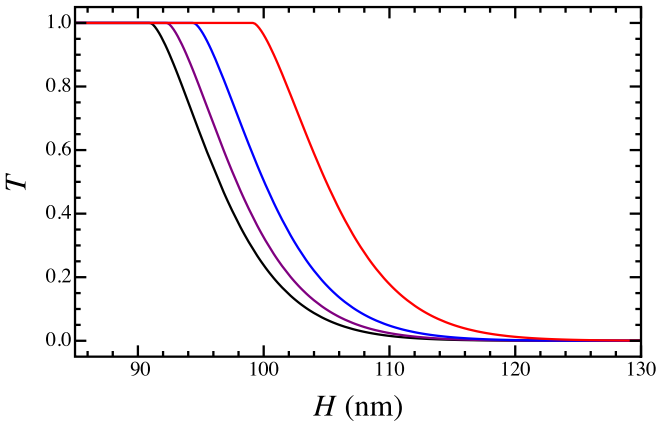

FIG. 7. Transmission coefficient of electrons in the $|K\downarrow\rangle$, $n = 0$, $l = 0$ state with magnetic-fields $B = 0$ T (black line), $B = 2.5$ T (purple line), $B = 5$ T (blue line), and $B = 10$ T (red line) in potential wells induced by nanopillars of height H in WSe_2 monolayers as given by the Fock-Darwin energy levels.

applications and scalability. In Sec. VI, possible methods of maintaining the spectra shown here for topographies more conducive to dot applications are discussed.

V. STATE LEAKAGE

One important comparison that needs to be made when comparing strain-induced potential wells in TMDs with other confinement methods is the state leakage probability. Demonstration of low leakage confinement by just out-of-plane straining of the monolayer crystal would open up the discussion for strained TMDs for quantum dots, whose purposes extend past SPEs, to single electron dots that may be coupled to other dots in a strain array for quantum information purposes. The transmission of an electron through a potential barrier, such as the ones discussed in this paper may be calculated by the semiclassical WKB method. The unitless transmission coefficient T is given in the following form:

$$T_{n,l}^{\tau,s} = \exp\left[-\frac{2}{\hbar}\int_{r_0}^{R}\sqrt{2m_{\text{eff}}^{\tau,s}\left[V(r) - E_{n,l}^{\tau,s}\right]}dr\right], \qquad (18)$$

where r_0 is the radial coordinate of the classical turning point at which (12) yields $V(r_0) = 0$, below which tunneling is not allowed, and above which the WKB approximation is valid. The full form of r_0 is given as follows:

$$r_0 = \sqrt{\frac{\sqrt{H}}{2\beta} + \frac{E_{n,l}^{\tau,s}(\sigma - 1)}{16h\beta\delta_c(1 - 2\sigma)}}. \qquad (19)$$

As can be seen from Figs. 7 and 8, the transmission coefficient of electrons out of the potential well in the classically allowed region ($E > 0$) is a function of the height of the deforming nanopillar exhibits a sharp cutoff point at which the electron may be assumed to be well confined. This sharp dependence of confinement with the nanopillar height aligns well with experimental results demonstrating the decreased SPE linewidth with increased nanopillar height [17]. As is also visible in Fig. 7 the WKB approximation breaks down at $T \approx 1$.

For states below the classically forbidden region ($E < 0$), the potential well, no tunneling outside the strained area should occur, unless aided by some thermal process. For MoS_2 this is very promising, as theoretically these strained dot arrays, if prepared properly and held at a sufficiently low temperature, should demonstrate low leakage. Additionally, the potential well depth may be tuned for state selection. If the height of the nanopillar is chosen such that the ground-state energy of one of Kramers pairs lies below the external zero-energy line, whereas the opposite Kramers pair lies above the line, with time, the dot will deliberately leak the unwanted Kramers pair, isolating only the desired Kramers pair. Additionally,

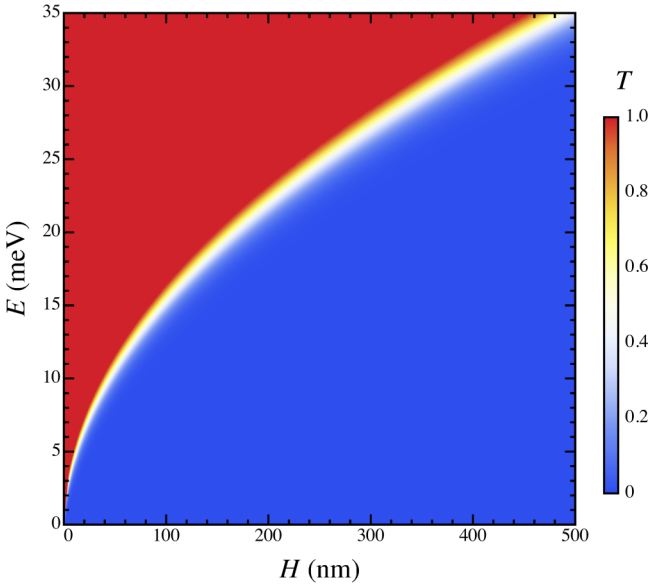

FIG. 8. Transmission coefficient spectrum of electrons in MoS_2 monolayers of energies E in potential wells induced by nanopillars of height H.

an external magnetic field may be applied perpendicular to the dot to further tune the dot to confine only one spin-valley combination within the low-energy Kramers pair. This state selection process may be difficult in MoS_2 since due to the relatively low spin-orbit splitting, high precision in the process may be required. However, TMD monolayers, such as WX_2 where the spin-orbit splitting is an order of magnitude greater and hole repulsion due to strain is still present, this Kramers isolation energy alignment may more easily be attained.

This demonstration of possible low leakage confinement in strain dots may be the key to opening up the possibility of strain-defined technologies in the TMD monolayers. For example, if an array of confining nanopillars may be grown underneath a TMD monolayer with patterned electronic gates atop the TMD, the strain would confine the electrons in the dots, whereas the gates may be used for local potential offsets to tune the coupling between each of the dots.

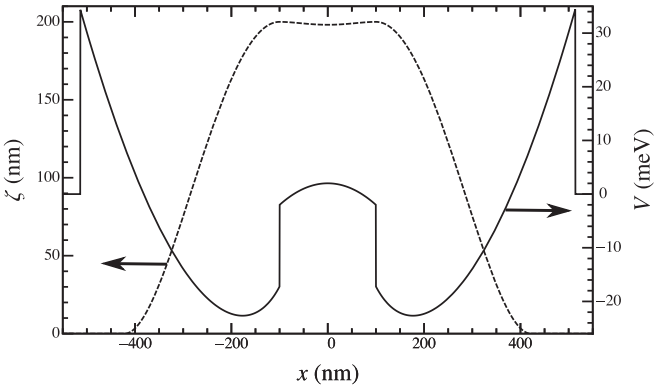

FIG. 9. Cross section along the x axis of the height-field ζ (dashed line) and potential V (solid line) induced in a WSe_2 monolayer by two 200-nm-high nanopillars separated 200 nm apart centered at $\mathbf{r} = (\pm 100\ \text{nm}, 0)$.

VI. DISCUSSION

Many possible electronic, photonic, spintronic, and valleytronic applications of TMD monolayers are in discussion as these materials offer a number of interesting physics. Strain-induced potential engineering is quickly becoming one of the many tools available for device implementation. Strain-defined quantum dots and wires in the monolayers can be used in combination with other confinement techniques, such as electronic gating and patterned etching or cutting of the monolayers. Additionally, strain engineering is also compatible with van der Waals few-layer heterostructure devices. This extensive toolbox of device engineering may allow for a new dimension of TMD devices to be explored. Here, we discuss the possibility of hybrid device implementations, building on the notion of strained well arrays introduced in Sec. V.

The previously introduced idea of an electrically tunable quantum dot array strained by nanopillars does present some problems, primarily; how would gating such an array affect the exploited mechanical properties of the TMD monolayer? Traditional metal contacts deposited on the TMD will certainly give regions of counterproductive stiffness to the monolayer, either limiting the strain response exploited in this paper, or increasing the probability of perforation or rupture. One possible solution is the replacement of the metal contacts with van der Waals heterostructure contacts. Some realizations of TMD-gated devices have used separate graphene sheet contacts either side of the device to tune the potential in lieu of or as intermediate interface with metal contacts [40,41]. These heterostructure would impact the mechanical properties to a certain extent, stiffening the Young's modulus and Poisson's ratio, but not enough to nullify the results presented here, additionally, the heterostructure should not affect the likelihood of monolayer damage. Positioning will be key in implementing a hybrid heterostructure gated-strain dot array, such as to correctly align nanopillars with the contacts. Thus, thin-finger-like graphene nanoribbons or even carbon nanotubes contacts would provide a positioning challenge while reducing the risk from perforation that etching provides.

If two nanopillars are placed close together with a TMD layered above them, the resulting potential would resemble two anharmonic wells with a near-square potential barrier of width equal to that of the distance between the nanopillars (Fig. 9). If carbon nanotube contacts are placed atop the TMD in between the nanopillars and on either side of the central strained region, then these contacts may be used to tune the barrier height between the two wells. In WSe_2 such a device could have interesting quantum optical applications. As it is known that similar strained regions in WSe_2 demonstrate quantum emitters, two dots joined by a tunable tunneling barrier would allow for a switchable coupling of the emitted photons from the device. A similar principle could be used with a MoS_2 single-particle quantum dot where a variable potential may be used tune the coupling constant of the dots, a necessary feature in scaling semiconducting spin or Kramers qubit implementations. This would allow for control over a quantum dot array while eliminating some of the charge noise compared to a similar system that is purely electrically confined [42] as fewer metallic gates would be needed to implement such a scheme.

The paper presented has focused on passively straining monolayer specifically with nanopillars grown from silica substrates. This method has been demonstrated to be useful for exciton coalescing, allowing for arrays of deterministically placed quantum emitters. For single-particle quantum dot applications, the width of such purely strain-induced wells may be too wide ($\sim$500 nm) and the well depths too shallow ($\sim$70 meV) to be experimentally useful. However, the method discussed in this paper is only straining the monolayers up to $\sim$0.5% as calculated from the trace of the strain tensor. This is a very comfortable level of strain for a TMD monolayer as these materials should be able to withstand straining up to $\sim$10% before rupture and $\sim$2% before transitioning to an indirect band gap in XS_2-type monolayers. More active straining of the TMDs could be implemented to engineer deeper smaller dots but only up to these material limits. One method of doing so while still using a nanopillar system could be from material selection of the substrate to foster greater van der Waals attraction between the substrate and the TMD or by electrostatic attraction of the TMD to a back gate underneath the substrate [43]. These methods have good compatibility as they allow for degrees of control over the system parameter $\beta = H/R^4$. AFM tip straining is another proposed method of tunable active straining for the TMD QD definition. This

method offers a more addressable height to the radius ratio of the dot at a greater risk of perforation and may not be as compatible with the on-chip hybrid systems discussed.

An additional possibility of hybrid implementation is impurity compensation in the TMD QD implementations. Experimentally, lattice defect density in the TMD monolayers is still problematic, randomly distributing local potential minima within a gated dot region. Similar to using such strained systems to deterministically place SPEs as opposed to rely on randomly distributed lattice defects, an additional layer of strain potential within a gated dot would limit the effect of the random strain defects.

Deterministic straining in combination with more conventional low-dimensional device control methods could potentially open up more device possibilities or improved implementations of devices in TMD monolayers. This further addition to the toolbox of low-dimensional material manipulation may help further bolster the already fertile field next-generation TMD-based technologies.

VII. SUMMARY

In this paper, an analytical description of the deformation topography and strain-induced potentials in monolayer TMD over nanopillars is derived from continuum-mechanical plate theory. We find a potential-well shape that is independent of the pillar height and a sharp drop-off of electron leakage with nanopillar height as given by a WKB theory analysis, matching observations in experiment while predicting the energy dependence of the emitted photons with nanopillar height. It can then be argued that the resulting strain potentials from such a setup have further use in hybrid design TMD devices, offering an additional layer of manipulation to a rapidly advancing field of technology. We propose a simple double quantum dot setup using adjacent nanopillars deforming a TMD with conducting graphene heterostructure contacts allowing a tunable coupling between two dots with fewer gates and thus lower electrical noise than conventional semiconducting quantum dot arrays and a method of compensating for lattice defects with controlled strain within a traditionally gated TMD QD.

ACKNOWLEDGMENTS

We acknowledge helpful discussions with A. David, A. Kormányos, A. Pearce, A. R.-P. Montblanch, M. Russ, V. Shkolnikov, and L. Sortino and funding through both the European Union (EU) by way of the ITN Spin-NANO Marie Sklodowska-Curie grant Agreement No. 676108 and the DFG through Grant No. SFB 767.

[1] Q. H. Wang, K. Kalantar-Zadeh, A. Kis, J. N. Coleman, and M. S. Strano, Nat. Nanotechnol. **7**, 699 (2012).
[2] A. Kumar and P. Ahluwalia, Eur. Phys. J. B **85**, 186 (2012).
[3] D. Xiao, G.-B. Liu, W. Feng, X. Xu, and W. Yao, Phys. Rev. Lett. **108**, 196802 (2012).
[4] A. Kormányos, V. Zólyomi, N. D. Drummond, and G. Burkard, Phys. Rev. X **4**, 011034 (2014).
[5] H.-J. Chuang, X. Tan, N. J. Ghimire, M. M. Perera, B. Chamlagain, M. M.-C. Cheng, J. Yan, D. Mandrus, D. Tománek, and Z. Zhou, Nano Lett. **14**, 3594 (2014).
[6] S. Jo, N. Ubrig, H. Berger, A. B. Kuzmenko, and A. F. Morpurgo, Nano Lett. **14**, 2019 (2014).
[7] S. Wachter, D. K. Polyushkin, O. Bethge, and T. Mueller, Nat. Commun. **8**, 14948 (2017).
[8] M.-L. Tsai, S.-H. Su, J.-K. Chang, D.-S. Tsai, C.-H. Chen, C.-I. Wu, L.-J. Li, L.-J. Chen, and J.-H. He, ACS Nano **8**, 8317 (2014).
[9] J. Feng, X. Qian, C.-W. Huang, and J. Li, Nat. Photonics **6**, 866 (2012).
[10] M. C. Lemme, F. H. Koppens, A. L. Falk, M. S. Rudner, H. Park, L. S. Levitov, and C. M. Marcus, Nano Lett. **11**, 4134 (2011).
[11] N. Zibouche, P. Philipsen, A. Kuc, and T. Heine, Phys. Rev. B **90**, 125440 (2014).
[12] M. Gmitra, D. Kochan, P. Högl, and J. Fabian, Phys. Rev. B **93**, 155104 (2016).
[13] X. Qian, J. Liu, L. Fu, and J. Li, Science **346**, 1344 (2014).
[14] Z. Gong, G.-B. Liu, H. Yu, D. Xiao, X. Cui, X. Xu, and W. Yao, Nat. Commun. **4**, 2053 (2013).
[15] K. F. Mak, K. He, J. Shan, and T. F. Heinz, Nat. Nanotechnol. **7**, 494 (2012).
[16] Y. Ye, J. Xiao, H. Wang, Z. Ye, H. Zhu, M. Zhao, Y. Wang, J. Zhao, X. Yin, and X. Zhang, Nat. Nanotechnol. **11**, 598 (2016).
[17] C. Palacios-Berraquero, D. M. Kara, A. R.-P. Montblanch, M. Barbone, P. Latawiec, D. Yoon, A. K. Ott, M. Loncar, A. C. Ferrari, and M. Atatüre, Nat. Commun. **8**, 15093 (2017).
[18] A. Branny, S. Kumar, R. Proux, and B. D. Gerardot, Nat. Commun. **8**, 15053 (2017).
[19] J. Kern, I. Niehues, P. Tonndorf, R. Schmidt, D. Wigger, R. Schneider, T. Stiehm, S. Michaelis de Vasconcellos, D. E. Reiter, T. Kuhn *et al.*, Adv. Mater. **28**, 7101 (2016).
[20] J. N. Coleman, M. Lotya, A. O'Neill, S. D. Bergin, P. J. King, U. Khan, K. Young, A. Gaucher, S. De, R. J. Smith *et al.*, Science **331**, 568 (2011).
[21] D. B. Velusamy, R. H. Kim, S. Cha, J. Huh, R. Khazaeinezhad, S. H. Kassani, G. Song, S. M. Cho, S. H. Cho, I. Hwang *et al.*, Nat. Commun. **6**, 8063 (2015).
[22] Y. Gong, V. Carozo, H. Li, M. Terrones, and T. N. Jackson, 2D Mater. **3**, 021008 (2016).
[23] C.-H. Chang, X. Fan, S.-H. Lin, and J.-L. Kuo, Phys. Rev. B **88**, 195420 (2013).
[24] D. M. Guzman and A. Strachan, J. Appl. Phys. **115**, 243701 (2014).
[25] Y. Wang, C. Cong, W. Yang, J. Shang, N. Peimyoo, Y. Chen, J. Kang, J. Wang, W. Huang, and T. Yu, Nano Res. **8**, 2562 (2015).
[26] M. Koperski, K. Nogajewski, A. Arora, V. Cherkez, P. Mallet, J.-Y. Veuillen, J. Marcus, P. Kossacki, and M. Potemski, Nat. Nanotechnol. **10**, 503 (2015).
[27] L. D. Landau, E. M. Lifshitz, A. M. Kosevich, and L. P. Pitaevskĭ, *Theory of Elasticity: Course of theoretical Physics* (Butterworth-Heinemann Ltd., Oxford, 1984), Vol. 7.
[28] G. L. Klimchitskaya, U. Mohideen, and V. M. Mostepanenko, Phys. Rev. A **61**, 062107 (2000).

[29] G. Wang, X. Marie, I. Gerber, T. Amand, D. Lagarde, L. Bouet, M. Vidal, A. Balocchi, and B. Urbaszek, Phys. Rev. Lett. **114**, 097403 (2015).
[30] R. Pisoni, Y. Lee, H. Overweg, M. Eich, P. Simonet, K. Watanabe, T. Taniguchi, R. Gorbachev, T. Ihn, and K. Ensslin, Nano. Lett. **17**, 5008 (2017).
[31] M. Brooks and G. Burkard, Phys. Rev. B **95**, 245411 (2017).
[32] S. Bertolazzi, J. Brivio, and A. Kis, ACS Nano. **5**, 9703 (2011).
[33] N. Morell, A. Reserbat-Plantey, I. Tsioutsios, K. G. Schädler, F. Dubin, F. H. Koppens, and A. Bachtold, Nano. Lett. **16**, 5102 (2016).
[34] K. Liu, Q. Yan, M. Chen, W. Fan, Y. Sun, J. Suh, D. Fu, S. Lee, J. Zhou, S. Tongay *et al.*, Nano. Lett. **14**, 5097 (2014).
[35] D. Çakır, F. M. Peeters, and C. Sevik, Appl. Phys. Lett. **104**, 203110 (2014).
[36] A. Splendiani, L. Sun, Y. Zhang, T. Li, J. Kim, C.-Y. Chim, G. Galli, and F. Wang, Nano. Lett. **10**, 1271 (2010).
[37] J. Huang, T. B. Hoang, and M. H. Mikkelsen, Sci. Rep. **6**, 22414 (2016).
[38] A. J. Pearce, E. Mariani, and G. Burkard, Phys. Rev. B **94**, 155416 (2016).
[39] H. Rostami, R. Roldán, E. Cappelluti, R. Asgari, and F. Guinea, Phys. Rev. B **92**, 195402 (2015).
[40] K. F. Mak and J. Shan, Nat. Photonics **10**, 216 (2016).
[41] S. Bertolazzi, D. Krasnozhon, and A. Kis, ACS Nano **7**, 3246 (2013).
[42] M. Russ, F. Ginzel, and G. Burkard, Phys. Rev. B **94**, 165411 (2016).
[43] C. Wong, M. Annamalai, Z. Wang, and M. Palaniapan, J. Micromechan. Microeng. **20**, 115029 (2010).